Green and Smart Mining Engineering 1 (2024) 67–75

Photocatalytic degradation of xanthates under visible light using heterogeneous CuO/TiO_2/montmorillonite composites

Sikai Zhao, Hong Xiao, Yunshuang Chen, Yaozhong Qi, Chenghao Yan, Ruixue Ma, Qiang Zhao, Wenbao Liu, Yanbai Shen*

School of Resources and Civil Engineering, Northeastern University, Shenyang 110819, China

ARTICLE INFO

Keywords:
TiO_2
CuO
Montmorillonite
Visible-light photocatalysis
Xanthates

ABSTRACT

Due to the significant demand for xanthate treatment in mineral effluents, photocatalytic techniques have emerged as one of the most promising solutions. In this study, a high-performance TiO_2/CuO/montmorillonite photocatalyst was prepared. In this configuration, TiO_2 was the classic photocatalytic material and CuO and montmorillonite were utilized to broaden the adsorption range of solar light and acted as carriers to support the photocatalyst. X-ray diffraction, scanning electron microscopy, transmission electron microscopy, and X-ray photoelectron spectroscopy were employed for the comprehensive characterization of the microstructure of the ternary photocatalyst. The results revealed that fine-sized TiO_2 and CuO nanoparticles were uniformly and tightly loaded on the montmorillonite layers. The photocatalytic properties of the photocatalyst were evaluated using sodium butyl xanthate as the target contaminant. For pristine TiO_2, ultraviolet (UV) light was required to effectively degrade sodium butyl xanthate. Meanwhile, the degradation reaction could be processed efficiently under visible light using the TiO_2/CuO/montmorillonite composite as the photocatalyst. Moreover, UV–visible diffuse reflectance spectroscopy, photoluminescence spectroscopy, and radical quench experiments were performed to elucidate the degradation process, and a possible degradation model and mechanism were proposed.

1. Introduction

Xanthates, characterized by their organosulfur composition, have undeniably revolutionized the processing techniques of sulfide minerals since their first introduction by Keller in 1925 [1]. Acting as collectors in froth flotation, xanthates display an outstanding affinity for metal sulfide surfaces, facilitating the formation of hydrophobic complexes essential for effective mineral separation [2]. Although some of the xanthates are adsorbed by mineral particles and flow to foam products during the froth flotation process, most of them remain in the flotation effluents, which raises serious environmental concerns and poses a significant threat to human health, underscoring a pressing need to address the potential ramifications [3,4].

To remove the adverse effects of organic pollutants in wastewater on the environment, different treatment techniques have been proposed, including physical, chemical, and biological approaches [5,6]. Physical treatment processes, such as adsorption, precipitation, and filtration, operate without the use of chemicals, providing a simple and highly efficient removal method for some solid contaminants. However, its cost and reusability limit its applicability. In addition, these methods can only achieve the enrichment and transfer of organic pollutants, falling short of complete degradation and elimination. Chemical treatment processes are the targeted addition of chemicals to remove or degrade contaminants and have high efficiency. However, the chemicals being added pose a risk of secondary pollution [7]. Meanwhile, biological methods use microorganisms for contaminant treatment, presenting natural techniques with advantages in cost and treatment effectiveness [8]. However, the slow processing speed requires large treatment sites, and microorganisms are sensitive to fluctuations in environmental conditions [9]. Therefore, to overcome these problems, innovative strategies beyond conventional techniques are increasingly demanded.

Recently, photocatalysis, a typical advanced oxidation technique, has garnered much attention as a promising approach for water remediation [10]. Under the principle of harnessing light to drive chemical reactions, photocatalysis shows remarkable promise for the

---

Peer review under the responsibility of Editorial Board of Green and Smart Mining Engineering.

* Corresponding author.

E-mail address: shenyanbai@mail.neu.edu.cn (Y. Shen).

https://doi.org/10.1016/j.gsme.2024.03.003
Received 28 December 2023; Received in revised form 21 January 2024; Accepted 1 February 2024
Available online 22 March 2024

degradation of organic contaminants, providing distinct advantages over traditional wastewater treatment methods, such as environmental friendliness, cost-effectiveness, and sustainability [11,12]. Photocatalysts play a key role in the photocatalysis process, determining the adsorption of light and the production of active radicals, which subsequently attack the organic pollutant and degrade it. Thus, the design and synthesis of novel photocatalysts for target pollutants have become a focus of the industrial application of photocatalysis.

Among the several photocatalytic materials studied to date, TiO_2 is widely regarded as an ideal candidate because of its thermal and chemical stability, low cost, high redox potential, and nontoxic nature [13,14]. However, when used as a high-performance photocatalyst, pristine TiO_2 faces two major challenges arising from its inherent properties. The first challenge is its low utilization efficiency of light. Because of its large band gap of 3.0–3.4 eV, TiO_2 can only adsorb light in wavelengths less than 387.5 nm, i.e., the UV range, which occupies 3%–5% of the solar light spectrum [15,16]. Thus, expanding the adsorption capacity to harness a broader range of the solar light spectrum is the main task in designing TiO_2-based photocatalysts. The second challenge is the fast recombination rate of photogenerated charge carriers [17]. Photocatalytic reactions are mainly induced by active radicals caused by photogenerated electrons and holes. The short lifetime of electron/hole pairs results in poor quantum efficiency and photocatalytic performance [18]. To address the above challenges, heterojunction formation and ion doping have been proven to be effective countermeasures. For example, Nguyen *et al.* [19] found that a suitable amount of Pd dopant can highly improve the photocatalytic activity of TiO_2 to methylene blue and methyl orange under UV light. Qu *et al.* [20] reported that $BiOCl/TiO_2$ exhibited much higher photocatalytic efficiency toward methyl orange under visible light than pristine TiO_2 and BiOCl.

In addition, the agglomeration and difficult recovery of TiO_2 photocatalysts are practical issues that need solving [21]. For a typical catalytic reaction, the crystal size of the catalyst is a crucial factor that influences catalytic performance, and in general, catalysts with smaller dimensions show higher catalytic activity [22]. Similarly, to ensure photocatalytic efficiency, TiO_2 photocatalyst powders must be highly dispersed and of fine size. Although the reduction in size can effectively improve the photocatalytic properties, the surface energy of the TiO_2 photocatalyst increases sharply with a decrease in physical size, resulting in a strong tendency of agglomeration of the photocatalyst and thus deteriorating the photocatalytic performance. Meanwhile, the separation of the fine-sized TiO_2 photocatalyst from the effluents after treatment for reuse is also a difficult and expensive process. To address these size-related challenges, researchers have developed different strategies [23,24]. A promising approach is to find appropriate carriers to support the fine TiO_2 photocatalyst [25]. In general, an effective carrier should have a large specific surface area with good adsorption ability for the target contaminants, thereby enhancing the photocatalytic reaction kinetics, and should be stable, nontoxic, and cheap. From this perspective, several materials have been studied as carriers of the TiO_2 photocatalyst, such as MoS_2 [26], metal–organic–frameworks [27], and graphene [28]. Among these, natural clay minerals have shown unique advantages and are considered the most promising ones [29,30]. Montmorillonite (MMT) is a layered silicate clay mineral with a 2:1-type dioctahedral structure [31] with the advantages of low cost, large specific surface, high chemical stability, and good dispersion suspension stability, making it a suitable carrier for the fabrication of functional composites such as photocatalysts [32]. The superiority of MMT carriers has been proven, and MMT can effectively enhance the photodegradation performance of TiO_2 to organics [33–35]. However, TiO_2/MMT composites only respond to UV light.

Therefore, this work aims to study the efficient degradation of xanthates in mineral effluents using a novel high-efficiency CuO/TiO_2/MMT (CTM) photocatalyst. On the one hand, the metal–oxide–semiconductor CuO is introduced to form a heterostructure with TiO_2. This design is to expand the light adsorption range from UV to visible light and slow down the recombination rate of the photogenerated electron–hole pairs. On the other hand, the layered MMT is selected as the carrier to support the CuO/TiO_2 heterostructure, which aims to mitigate the adverse effects of the fine size of the photocatalyst. The microstructure and photocatalytic performance of the proposed photocatalyst for xanthates are studied, and the mechanism for the enhanced photocatalytic properties is also discussed.

2. Experimental

2.1. Chemicals

MMT, copper(II) nitrate trihydrate ($Cu(NO_3)_2{\cdot}3H_2O$, AR), and 1,4-benzoquinone (BQ, AR) were obtained from Sinopharm Chemical Reagent Co., Ltd. Sodium ethyl xanthate (SEX), sodium isopropyl xanthate (SIPX), sodium isoamyl xanthate (SIAX), and sodium butyl xanthate (SBX) were procured from Tieling Flotation Reagents Co., Ltd. TiO_2 powder (CP), ethylenediaminetetraacetic acid disodium salt (EDTA-2Na, AR), and isopropanol (IPA, AR) were obtained from Shanghai Macklin Biochemical Co., Ltd., Shanghai Aladdin Biochemical Technology Co., Ltd., and Tianjin Kemiou Chemical Reagent Co., Ltd., respectively.

2.2. Materials synthesis

Before constructing the CTM ternary structure, the TiO_2/MMT composites were first prepared by grounding a mixture of 0.8 g of TiO_2 powder, 0.2 g of MMT powder, and 3 mL of ethanol for 30 min in an agate mortar, followed by drying to evaporate the ethanol. The dried material was then transferred to an alumina crucible and annealed at 400 °C for 6 h in a tube furnace at 10 °C/min. After cooling down naturally to around 30 °C, the TiO_2/MMT composites were obtained.

To prepare the CTM heterogeneous materials, 0.5 g of as-prepared TiO_2/MMT and a predefined amount of ($Cu(NO_3)_2{\cdot}3H_2O$ were ground in an agate mortar for 20 min with ethanol (adding 2 mL in the first and second 10 min of the grinding process). Afterward, the mixture was dried and further ground for another 10 min and then annealed in a tube furnace at 5 °C/min. Finally, the resulting samples were washed with ethanol and water and dried at 60 °C to yield CTM. In this study, CTM composites with different Cu/Ti molar ratios were prepared and studied. CTM composites with Cu/Ti molar ratios of 5%, 10%, 15%, and 20% were denoted as CTM-5%, CTM-10%, CTM-15%, and CTM-20%, respectively.

2.3. Materials characterizations

The crystal structure of the prepared materials was characterized by X-ray diffraction (XRD, XRD-7000, Shimadzu) using Cu K_α at $\lambda = 0.15406$ nm. The microstructure was observed by scanning electron microscopy (SEM, ZEISS Ultra Plus) and transmission electron microscopy (TEM, JEM-F200) at accelerating voltages of 20 and 200 kV, respectively. Surface properties were analyzed by X-ray photoelectron microscopy (XPS, ESCALAB 250Xi) using monochromatic Al K_α radiation ($h\nu = 1486.6$ eV) with an operating voltage of 14.6 eV. Brunauer–Emmett–Teller (BET) surface area and pore size distribution analysis was conducted using a QUADRASORB SI analyzer at 196 °C. UV–visible diffuse reflectance spectroscopy (UV–Vis DRS) was performed using a UV-3600 spectrophotometer with $BaSO_4$ as a reference. Photoluminescence spectroscopy (PL) was performed on an FLS1000 spectrometer using an excitation wavelength of 325 nm at room temperature.

2.4. Photocatalytic testing

Evaluation of the photocatalytic properties of the prepared photocatalysts was conducted by photodegradation tests of SBX, a typical xanthate, in a Princeton PL-03 reactor with a 350 W xenon lamp and

UV cutoff filter ($\lambda > 400$ nm), and then, the SBX concentration in the solution was determined by UV–Vis analysis. The experimental details are shown in the Supplementary Information (Fig. S1). Briefly, the prepared photocatalyst was dispersed in 50 mL of SBX solution in a quartz batch reactor. Before photoirradiation, the suspension was stirred in the dark for 30 min to establish adsorption–desorption equilibrium. Then, light was turned on and the photocatalytic reaction was maintained for 40 min with continuous magnetic stirring and air pumping into the reactor. During both the dark and reaction processes, 4 mL of the sample was taken from the suspension at given time intervals and then centrifuged at 10000 r/min for 3 min. The supernatant was used for UV–Vis analysis, and the SBX concentration was determined by absorbance at 301 nm.

3. Results and discussion

3.1. Characterizations

For the photocatalyst of the CTM composites in this study, CuO and TiO_2 play the primary role in the photoreaction, and MMT serves as the support of the CuO and TiO_2 nanoparticles. In general, the interfacial and photocatalytic properties of the photocatalyst considerably depend on the proportion of CuO and TiO_2 in the photocatalyst. Thus, photocatalysts with different CuO and TiO_2 ratios were prepared and studied for better photocatalytic performance. Fig. 1 displays the XRD patterns of the different samples. For the TiO_2/MMT binary sample, the MMT peaks were suppressed, and the TiO_2 peaks emerged. Two types of TiO_2 crystal structures, namely, anatase (ICCD #21–1272) and rutile (ICCD #21–1276), can be observed, demonstrating the formation of a mixture phase of TiO_2 [36,37]. Previous studies have reported the advantages of the TiO_2 mixture phase in photocatalysis compared with the single phase [38,39]. After introducing the Cu element (CTM samples), the CuO peaks (ICCD #80–1916) appear and intensify gradually with increasing Cu/Ti molar ratio [40].

Pristine MMT is a typical two-dimensional lamellar structured clay mineral (Fig. S2), which gives it special advantages for photocatalyst loading and makes it a promising carrier. Fig. 2(a) presents the SEM image of the TiO_2/MMT binary composite. The TiO_2 particles are sphere-like with a diameter of around 25 nm and are closely attached to the surfaces of the MMT layers. The CTM ternary composites with different Cu/Ti mass ratios in Fig. 2(b–f) indicate that further introduction of Cu series compounds clearly increases particle aggregation and surface roughness of the samples. In addition, increasing the Cu/Ti molar ratio increases the size of the particles. TEM was applied to further examine the microstructure of the sample. The TEM images of the CTM-40% sample in Fig. 2(g, h) confirm the ternary structure of the prepared CTM sample, where TiO_2 and CuO with good crystallinity are uniformly and tightly combined onto the surfaces of MMT lamellae, demonstrating the good supporting ability of the MMT. The CuO nanoparticles have a fine size of ca. 10 nm in diameter, giving them high surface activity and facilitating carrier transfer between TiO_2 and CuO, which is beneficial for photocatalytic reactions. Fig. 2(i–l) displays the elemental mapping images of the CTM-40% sample, verifying the presence of Al, Si, Ti, and Cu elements in the sample and showing good dispersion of TiO_2 and CuO on the surfaces of MMT.

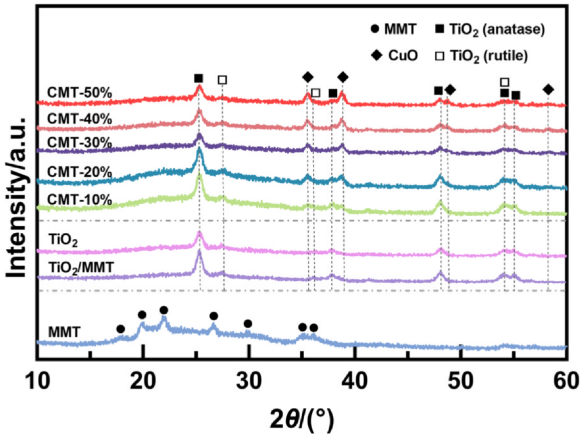

Fig. 1. XRD patterns of the different samples.

Fig. 3 presents the N_2 adsorption/desorption isotherms and the Barrett–Joyner–Halenda (BJH) pore size distribution plots. The MMT, TiO_2, TiO_2/MMT, and CTM-40% materials show typical Type IV adsorption isotherm and H3 hysteresis loop characteristics (Fig. 3(a)), demonstrating that the pores on the surfaces of these materials are mainly present as mesopores. The pore size mainly distributes between 3 and 32 nm (Fig. 3(b)). This structure is advantageous to increase the number of adsorption channels and catalytic sites on surfaces of materials, thereby improving photocatalytic performance.

Table 1 summarizes the pore characteristics of the materials. TiO_2/MMT exhibits a higher specific surface area than the individual MMT and TiO_2, while its pore volume is significantly larger than that of MMT but is near that of TiO_2, indicating that the TiO_2 nanoparticles with high specific surface area are uniformly dispersed on the surfaces of the MMT carriers. Compared with TiO_2/MMT, CTM-40% exhibits a decreased specific surface area, but its total pore volume, mesopore volume, and average pore size are all larger than those of TiO_2/MMT. The SEM images in Fig. 2 reveal that incorporating CuO results in the agglomeration of TiO_2 particles. This agglomeration occupies and obstructs some pre-existing mesopores while forming new pathways, thus influencing the specific surface area and pore characteristics of the composite materials.

Fig. 4 depicts the XPS spectra of the CTM-40% composites. In Fig. 4(a), the survey scan spectrum proves the presence of Cu, Ti, and Si elements in the sample, which originate from the CuO, TiO_2, and MMT components, respectively. Five distinct peaks in the Cu 2p high-resolution spectrum in Fig. 4(b) are observed, of which the primary 933.60 and 953.45 eV peaks are attributed to Cu $2p_{3/2}$ and Cu $2p_{1/2}$, respectively, and the rest are satellite peaks. Fig. 4(c) shows the spectrum in the binding energy range of 454–470 eV, where two peaks at 464.26 and 458.60 eV are associated with Ti $2p_{1/2}$ and Ti $2p_{3/2}$, respectively. Two peaks are observed in the O 1s narrow scan spectrum in Fig. 4(d), i.e., 529.84 and 532.25 eV, which are assigned to the lattice oxygen in the complex material and the oxygen adsorbed on the surface of the material, respectively [41,42].

3.2. Photocatalytic properties

A typical xanthate, SBX, was selected as the target contaminant for evaluation of the photocatalytic performance of the developed photocatalysts. Fig. 5 plots the degradation efficiency and kinetic curves of CTM photocatalysts with different Cu/Ti molar ratios under visible light. Clearly, the TiO_2/MMT photocatalyst can only effectively degrade SBX under UV light (Figs. S3 and S4, and Fig. 5(a)), while a small drop in SBX concentration under visible light is mainly caused by the adsorption effect of the TiO_2/MMT photocatalyst. This phenomenon is expected and consistent with the fact that TiO_2 has a large band gap and requires photons with higher energy to be excited. Introducing CuO, a small bandgap semiconductor (~ 1.3 eV) [43,44], the photocatalytic performance of the photocatalyst is significantly improved, showing that the constructed CuO/TiO_2 heterostructure can effectively broaden the light utilization range of TiO_2 from UV light to visible light. Moreover, the CTM ternary samples show a much higher SBX adsorption capacity than the TiO_2/MMT binary sample, which can effectively promote the photocatalytic process by increasing the local concentration of the target contaminants near the photocatalyst, further demonstrating the superiority of the CTM photocatalyst in SBX photodegradation treatment. In comparison, the CTM-40% sample exhibited the highest degradation efficiency and fasted degradation rate; thus, the CTM-40% sample was selected for further experiments.

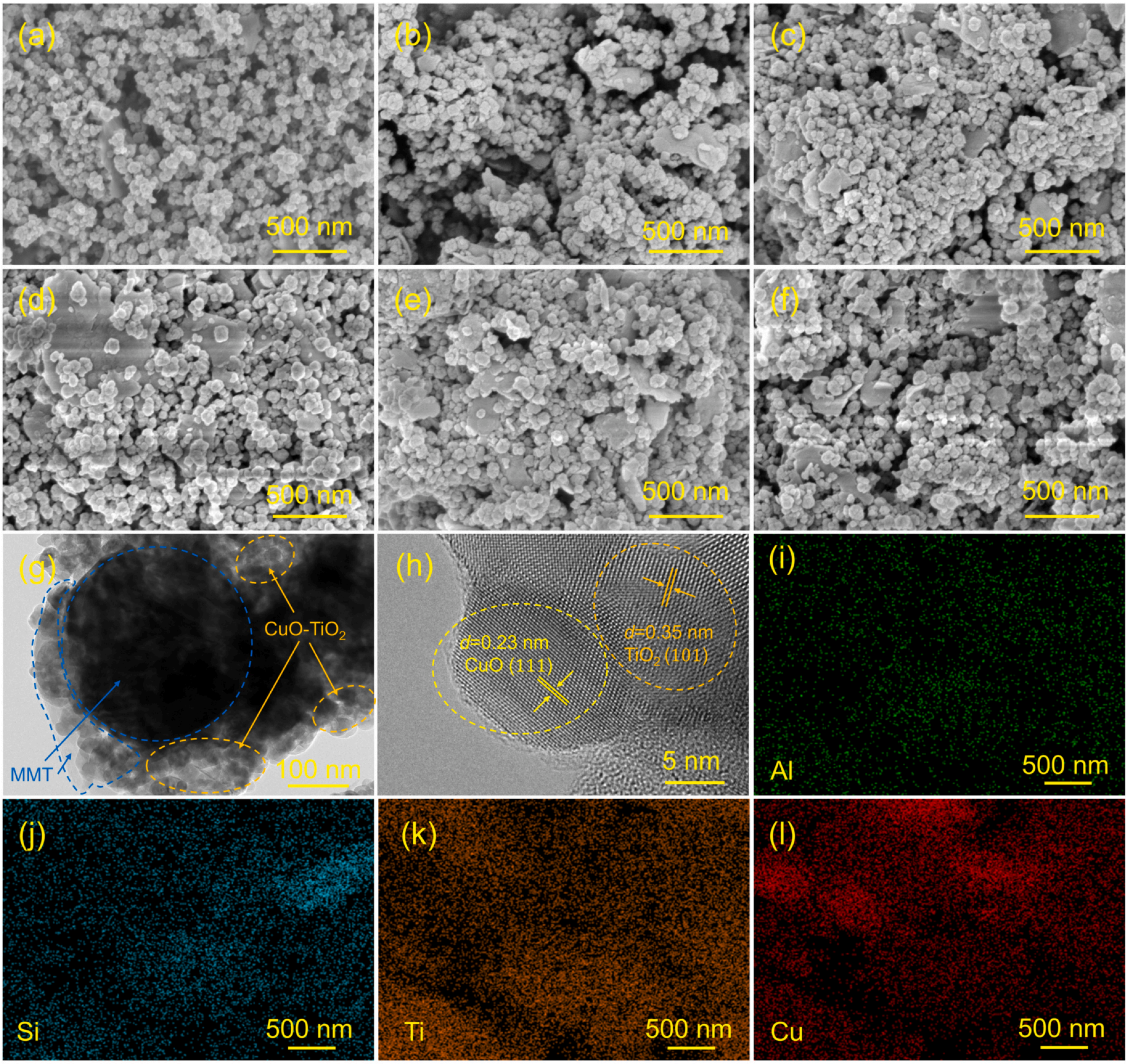

Fig. 2. SEM images of (a) TiO$_2$/MMT, (b) CTM-10%, (c) CTM-20%, (d) CTM-30%, (e) CTM-40%, and (f) CTM-50%. (g) TEM image, (h) HRTEM image, (i–l) elemental mapping of the CTM-40% sample.

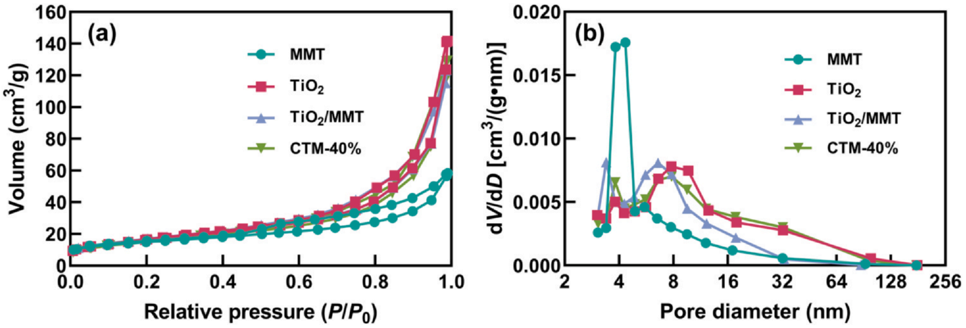

Fig. 3. (a) N$_2$ adsorption/desorption isotherms and (b) BJH pore size distribution plots of the samples.

Fig. 6 illustrates the photocatalytic degradation performance of CTM-40% at different dosages to 20 mg/L SBX. From Fig. 6(a), the adsorption–desorption kinetics of SBX on the surfaces of CTM reach a quasi-equilibrium state within 30 min of dark reaction, and the adsorption capacity increases with increasing CTM-40% dosage. After visible-light irradiation is turned on, the degradation efficiency of SBX

Table 1
Pore textural properties of the samples.

Sample	S_{BET} (m^2/g)[a]	V (cm^3/g)[b]	D (nm)[c]	V_{meso} (cm^3/g)[d]
MMT	51.55	0.0902	6.9969	0.0664
TiO_2	58.68	0.2191	14.9382	0.1486
TiO_2/MMT	59.67	0.1911	12.8077	0.1403
CTM-40%	53.93	0.2000	14.8358	0.1525

[a] Specific surface area calculated by the BET method;

[b] Pore volume obtained from the BJH desorption cumulative volume;

[c] Average pore diameter evaluated using desorption isotherms and the NJH model;

[d] Mesopore volume obtained from the BJH desorption pore distribution report.

increases with prolonged time and significantly improves with increasing CTM-40% dosage due to the increased adsorption and reaction active sites. Fig. 6(b) shows the corresponding degradation kinetic curves, demonstrating that all degradation processes follow the first-order kinetics model and that the apparent rate constant of the degradation reaction initially increases rapidly and then decreases gradually with increasing catalyst dosage. At lower catalyst dosages, the number of active radicals generated by the catalyst is the key factor that determines SBX degradation. Therefore, increasing the dosage of the photocatalyst in a certain range can effectively increase the active radical concentration in the solution, thereby promoting the rapid progress of the photocatalytic degradation reaction. However, when the dosage of the photocatalyst is further increased, the degradation efficiency decreases, which is mainly ascribed to the increased turbidity of the reaction system. Although generally, the higher the amount of photocatalyst, the higher the degradation rate, the SBX degradation efficiency is greater than 98% within 40 min at a CTM-40% dosage of 0.2 g/L with the fastest degradation rate; thus, 0.2 g/L is the optimal CTM-40% dosage in terms of cost-effectiveness.

Fig. 7 displays the photodegradation performance of the prepared CTM-40% photocatalyst with different SBX concentrations. With increasing initial SBX concentration, photocatalytic degradation efficiency and apparent rate constant of the degradation process decrease gradually. When the initial SBX concentration is only 20 mg/L, the degradation efficiency remains above 98% for 40 min. However, it decreases sharply to 64.4% with the further increase of SBX concentration to 40 mg/L. For a specific amount of photocatalyst, the active sites provided and the active radicals generated by the photocatalysts are limited within a certain time; thus, a higher SBX concentration would prolong the time required for complete degradation. Thus, for photocatalytic process design in practical applications, the pollutant solution should be well controlled in terms of cost and degradation efficiency.

For the froth flotation separation of sulfide ores, different types of xanthates were employed based on ore properties. Fig. 8 presents the photocatalytic properties of CTM-40% for the four most widely used xanthates: SEX, SIPX, SBX, and SIAX. Clearly, the photocatalyst shows good degradation performance for all xanthates, obtaining degradation efficiencies of 95.9%, 97.5%, 98.3%, and 98.7% for SEX, SIPX, SBX, and SIAX, respectively, at 40 min. Interestingly, xanthates with branched hydrocarbon chains are more easily degraded than those without branched chains, which can be ascribed to the lower chemical stability of xanthates with branched chains. Moreover, with increasing molecular weight of the xanthates, the degradation rate increases due to the influence of complex chain structures on molecular polarity; thus, xanthate molecules with smaller weights are more prone to adsorption on the photocatalyst surface, thus facilitating the degradation process.

Fig. 9 displays the change in SBX degradation efficiency by CTM-40% in the four continuous degradation cycles. The degradation efficiency shows a certain degree of decline with an increasing number of reuse cycles but is still above 90% after four reuse cycles, showing good stability and reproducibility of the photocatalyst during the photodegradation process.

3.3. Degradation mechanism

Fig. 10(a) plots the real-time UV–Vis spectra used to evaluate the degradation of SBX by the synthesized CTM-40% photocatalyst. Before the reaction, two characteristic peaks at 226 and 301 nm can be clearly

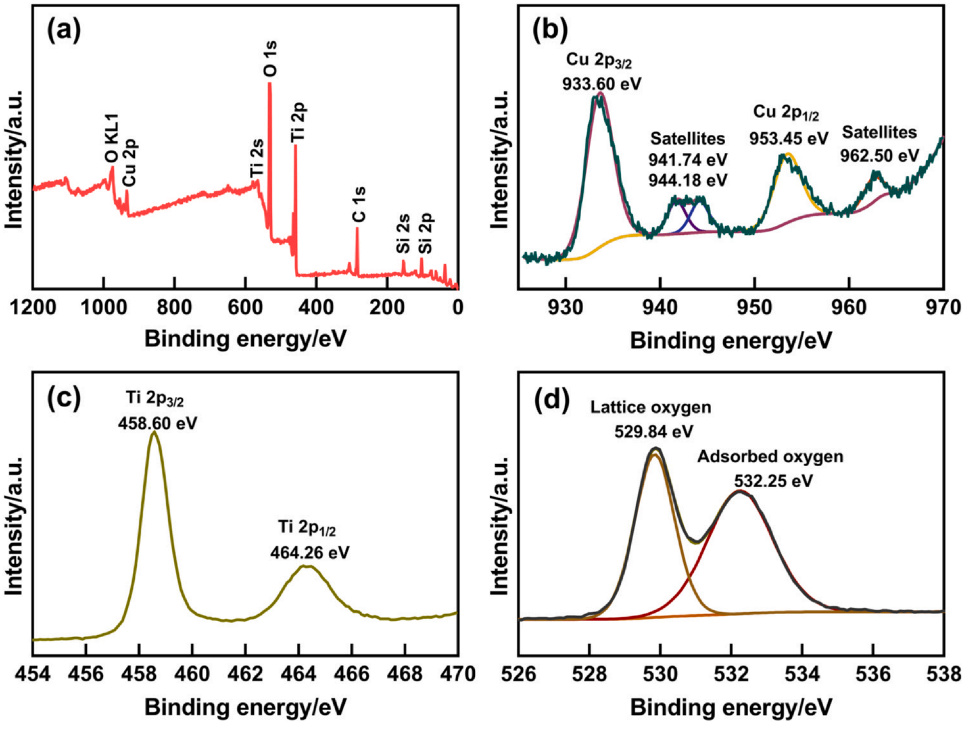

Fig. 4. XPS spectra of CTM-40% composites: (a) full scan spectrum, (b) Cu 2p spectrum, (c) Ti 2p spectrum, and (d) O 1s spectrum.

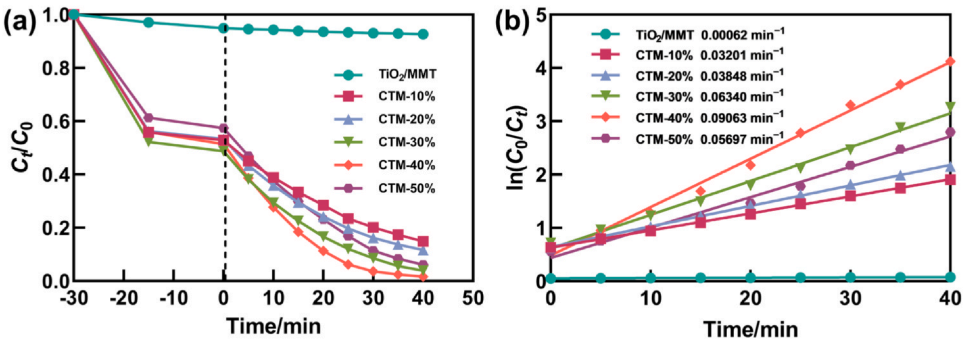

Fig. 5. (a) Photocatalytic degradation efficiency curves and (b) kinetic curves of TiO_2/MMT and CTM samples with different Cu/Ti molar ratios. C_0 and C_t represent the concentration (mg/L) of SBX at initial and t time, respectively.

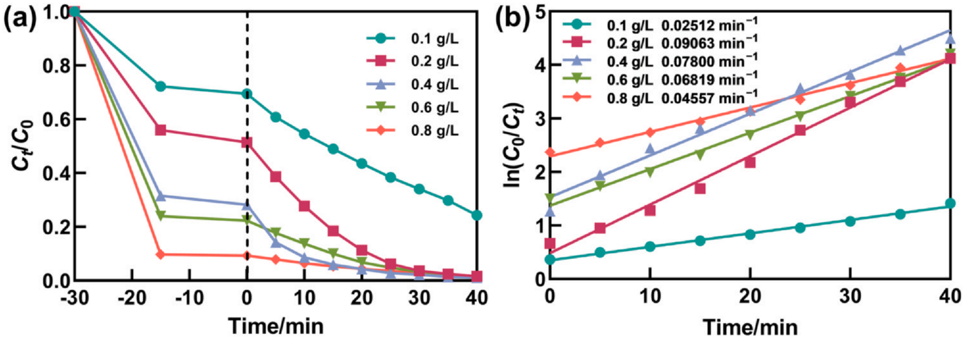

Fig. 6. Effect of the CTM-40% composite dosage on the degradation of SBX: (a) degradation efficiency curves and (b) degradation kinetic curves.

observed, revealing a sharp decline in the first 15 min, demonstrating the good SBX adsorption property of CTM-40%. In the next 15 min, the intensity of the two peaks only slightly decreases because the adsorption–desorption equilibrium is gradually reached. Once illuminated by visible light, the peak intensities reduce rapidly with prolonged time, and no obvious peak is detected after 40 min, showing that the prepared CTM-40% catalyst has a good photocatalytic performance and that SBX can be almost completely degraded within 40 min. To elucidate the reaction process, active radical quenching experiments were conducted using BQIPA and EDTA-2Na as the quenchers of $\cdot O_2^-$, $\cdot OH$, and h^+. The results are shown in Fig. 10(b), showing that IPA displays little effect on the degradation efficiency while the addition of BQ and EDTA-2Na significantly reduces the degradation efficiency with BQ, showing that $\cdot O_2^-$ and h^+ are the main active radicals during the photodegradation process of SBX and $\cdot O_2^-$ makes the primary contribution.

To determine the photoadsorption ability and bandgaps of the different samples, UV–Vis DRS was employed, and the results are shown in Fig. 11(a, b). The optical adsorption threshold of the pristine TiO_2 takes place at 412 nm, whereas that of TiO_2/MMT extends to 420 nm and exhibits evaluated absorbance in the 200–300 nm region, indicating that the MMT clay mineral not only serves as the support to TiO_2 particles but also improves the UV-light adsorption capacity of TiO_2. Furthermore, once CuO is introduced to form the CTM ternary composites, a significant redshift to 462 nm is evident, together with outstanding absorbance performance in the 400–600 nm range, suggesting that CuO addition effectively broadens the adsorption range from UV to visible light. Using the Tauc plot method [45,46], the bandgap widths of TiO_2, TiO_2/MMT, and CTM-40% are evaluated and shown in Fig. 11(b). CTM-40% shows a much smaller bandgap (1.90 eV) than TiO_2 (2.90 eV) and TiO_2/MMT (2.80 eV). The narrowed bandgap greatly lowers the energy threshold for generating photoinduced electron/hole pairs and improves the visible-light response.

Fig. 11(c) displays the PL spectra of the different samples. The pristine TiO_2 achieves the strongest PL signal intensity, consistent with the intrinsic characteristic of the high photogenerated electron/hole recombination rate of TiO_2. Meanwhile, for the TiO_2/MMT binary composite, the PL signal intensity significantly decreases, showing that the MMT clay mineral can also effectively suppress the photogenerated electron/hole recombination rate of the TiO_2 nanoparticles, apart from the role of a carrier and light adsorption capacity enhancer. Moreover, the CTM-40% ternary composite exhibits the weakest PL signal intensity. Evidently, the incorporation of CuO and the formation of the

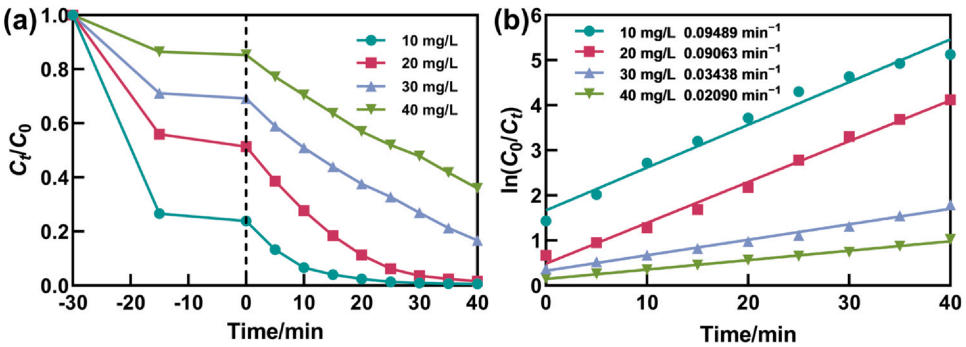

Fig. 7. Effect of the initial concentration of CTM-40% composite on SBX degradation: (a) degradation efficiency curves and (b) corresponding kinetic curves.

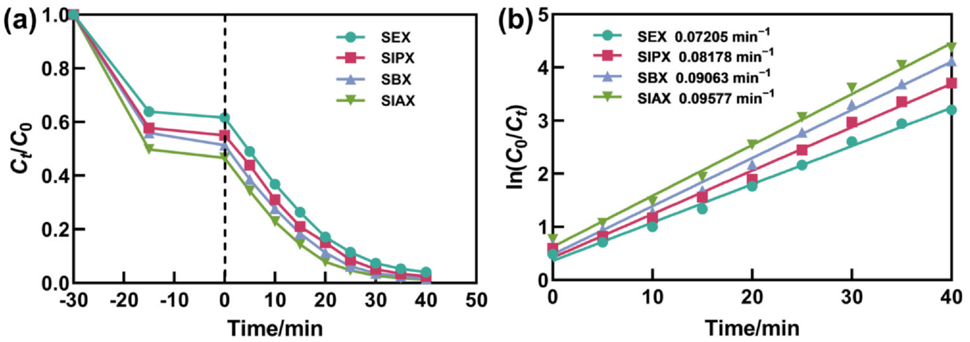

Fig. 8. Effect of degradation of the different xanthates over the CTM-40% composite: (a) degradation efficiency curves and (b) degradation kinetic curves.

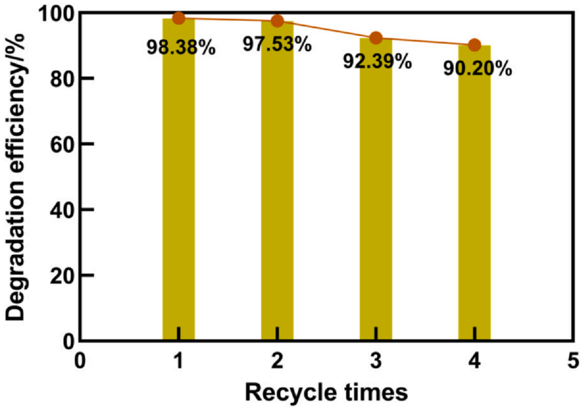

Fig. 9. Reproducibility of the degradation of SBX over the CTM-40% composites.

CuO–TiO_2 heterostructure further decrease the electron/hole recombination rate, thus substantially contributing to the remarkable photocatalytic properties of the CTM-40% composite.

Based on the previously reported data and the analysis above, the band structure and the possible photocatalytic degradation mechanism of the CTM-40% photocatalyst are illustrated in Fig. 12. In terms of the constitution and structure of the CTM-40% photocatalyst, because TiO_2 (4.70 eV) has a much smaller work function than CuO (5.31 eV), when they come into close contact in the CTM-40% composite, the electrons in the TiO_2 conduction band diffuse to the CuO conduction band until their Fermi levels become equal [47]. Thus, a built-in electric field is formed near the contact region, and a type-II heterojunction is established [48]. Due to CuO addition and formed CuO–TiO_2 heterojunction, the CTM-40% photocatalyst displays a good visible-light response. Under visible-light irradiation, electrons in the valence bands of TiO_2 and CuO are excited to their conduction bands and leave holes in the valence bands. Driven by the built-in field in the CuO–TiO_2 type-II heterojunction, the photogenerated electrons in the CuO conduction band drift to the TiO_2 conduction band, while the photogenerated holes in the TiO_2 valence band drift to the CuO valence band. These carrier movements effectively separate the photogenerated carriers and improve their lifetimes, enabling CuO and TiO_2 to be the active sites for oxidization and reduction, respectively. Afterward, the photogenerated e^- react with the O_2 molecules adsorbed on the surfaces of the CTM-40% photocatalyst to form $\cdot O_2{}^-$ radicals, which are strong oxidants and further react with xanthates to degrade them into nontoxic inorganics. In addition, because both the TiO_2 and CuO valence band potentials in the photocatalyst are lower than the potential of OH/OH, the photogenerated holes cannot effectively oxidize H_2O or –OH into OH radicals [42], in agreement with the active radical quenching experimental results in Fig. 10(b), which show that ·OH radicals have a slight effect on the degradation efficiency. In conclusion, the dominant active species for xanthate degradation is $\cdot O_2{}^-$, while h^+ also plays an important role. The possible degradation reactions are expressed in Eqs. (1)–(4).

$$CuO + h\nu \rightarrow e_{CB}^- + h_{VB}^+ \tag{1}$$

$$TiO_2 + h\nu \rightarrow e_{CB}^- + h_{VB}^+ \tag{2}$$

$$e_{CB}^- + O_2 \rightarrow \cdot O_2^- \tag{3}$$

$$C_2H_9OCSS^- \xrightarrow{\cdot O_2^-,\ \ h_{VB}^+} CO_2 + H_2O + \cdots \tag{4}$$

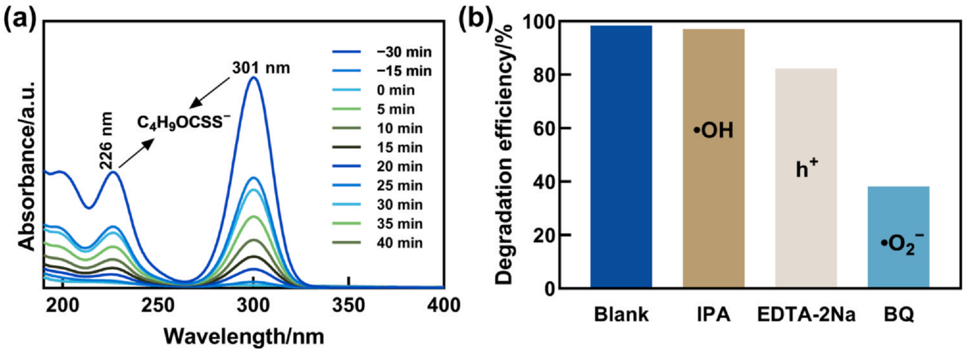

Fig. 10. (a) Real-time absorbance curves of the CTM-40% photocatalyst in the degradation process of SBX. (b) Effect of different scavengers on the photocatalytic degradation by CTM-40% to SBX.

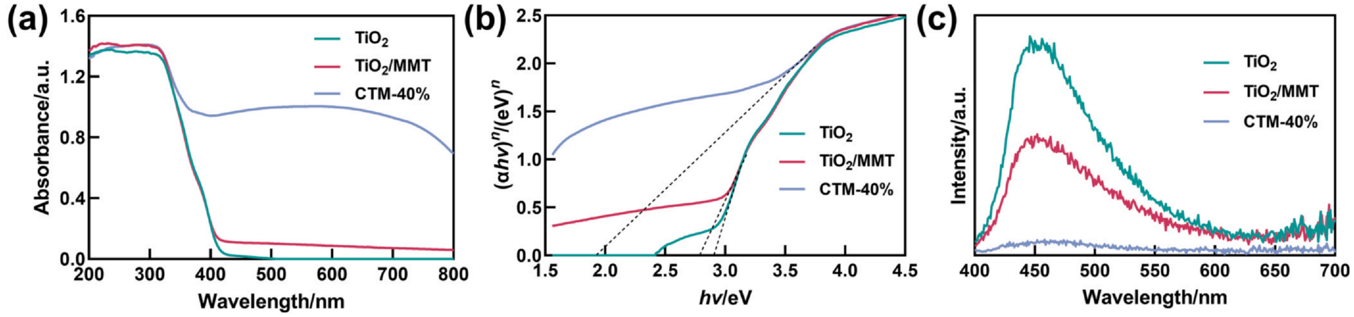

Fig. 11. (a) UV–Vis DRS, (b) bandgaps, and (c) PL spectra of TiO_2, TiO_2/MMT, and CTM-40%.

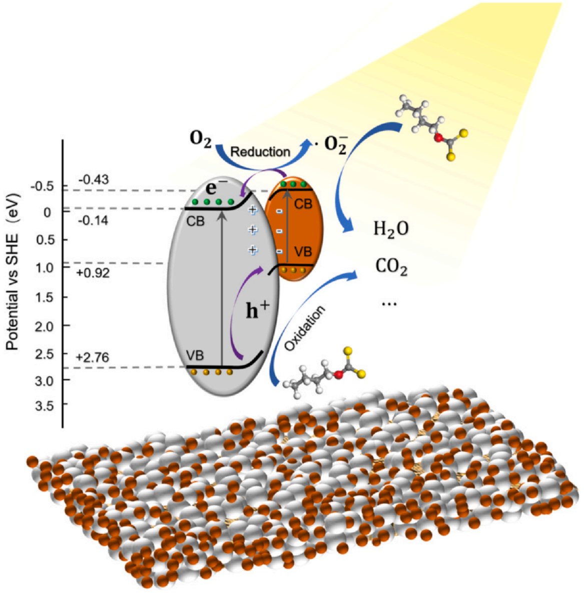

Fig. 12. Photodegradation mechanism of SBX over the CTM-40% photocatalyst under visible light. CB and VB are conduction band and valence band, respectively.

4. Conclusion

A novel ternary photocatalyst of TiO_2, CuO, and MMT was successfully prepared by impregnation–pyrolysis. TiO_2 and CuO nanoparticles with sizes of ca. 25 and ca. 10 nm, respectively, are closely combined and uniformly loaded on the surfaces of the MMT layers. TiO_2 nanoparticles have a mixed anatase and rutile structure, while CuO nanoparticles have a monoclinic crystal structure. The prepared CTM ternary composites display outstanding photodegradation performance toward SBX under visible light. At a Cu/Ti molar ratio of 40%, the CTM-40% photocatalyst obtains a high degradation efficiency of 98.38% for 40 min under the following conditions: 20 mg/L photocatalyst dosage, 20 mg/L SBX initial concentration, and 350 W solar light intensity. During the photodegradation process, $\cdot O_2^-$ and h^+ are the main active species, with $\cdot O_2^-$ making the primary contribution. The formation of the CuO–TiO_2 heterostructure and the introduction of MMT clay minerals are the critical reasons for the superior photocatalytic performance of the CTM composite over pristine TiO_2, which not only narrows the bandgap and broadens the light utilization range but also effectively suppresses the recombination rate of the photogenerated electron/hole pairs.

CRediT authorship contribution statement

Sikai Zhao: Conceptualization, Writing – original draft. **Hong Xiao, Yunshuang Chen, Yaozhong Qi, Chenghao Yan, Ruixue Ma:** Investigation. **Qiang Zhao, Wenbao Liu:** Writing – review & editing. **Yanbai Shen:** Conceptualization, Supervision, Writing – review & editing.

Declaration of Competing Interest

Yanbai Shen is an editorial board member for this journal and was not involved in the editorial review or the decision to publish this article. The authors declare that they have no known financial interests or personal relationships that could have appeared to influence the work reported in this paper.

Acknowledgements

This work was financially supported by the National Natural Science Foundation of China (Nos. 52274255 and 51674067), National Key R& D Program of China (No. 2020YFB2008702), Fundamental Research Funds for the Central Universities (Nos. N2301003, N2201008, N2201004, and N2301025), Liaoning Revitalization Talents Program (No. XLYC1807160), Postdoctoral Foundation of Northeastern University, Young Elite Scientists Sponsorship Program by CAST (No. 2022QNRC001), and China Postdoctoral Science Foundation (No. 2022M720025).

Appendix A. Supporting information

Supplementary data associated with this article can be found in the online version at doi:10.1016/j.gsme.2024.03.003.

References

[1] C.S. Zhou, A. Bahr, G. Schwedt, Studies on the HPLC determination of xanthates via copper(I) xanthates and dixanthogens, Z. Anal. Chem. 334 (6) (1989) 527–533.

[2] J.Q. Yuan, S.Q. Li, Z. Ding, J. Li, A.M. Yu, S.M. Wen, S.J. Bai, Treatment technology and research progress of residual xanthate in mineral processing wastewater, Minerals 13 (3) (2023) 435.

[3] M. Jiang, M.H. Zhang, L.Z. Wang, Y.W. Fei, S. Wang, A. Núñez-Delgado, A. Bokhari, M. Race, A. Khataee, J. Jaromír Klemeš, L.B. Xing, N. Han, Photocatalytic degradation of xanthate in flotation plant tailings by TiO_2/graphene nanocomposites, Chem. Eng. J. 431 (2022) 134104.

[4] Z.Z. Bian, Y.L. Feng, H.R. Li, H. Yu, H. Wu, Adsorption-photocatalytic degradation and kinetic of sodium isobutyl xanthate using the nitrogen and cerium co-doping TiO_2-coated activated carbon, Chemosphere 263 (2021) 128254.

[5] J.Q. Yuan, Z. Ding, X. Gong, A.M. Yu, S.M. Wen, S.J. Bai, Degradation of residual xanthate in flotation tailing wastewater by activated H_2O_2 with natural ilmenite: A heterogeneous fenton-like reaction catalyzed at natural pH, Sep. Purif. Technol. 332 (2024) 125819.

[6] G.C. Molina, C.H. Cayo, M.A.S. Rodrigues, A.M. Bernardes, Sodium isopropyl xanthate degradation by advanced oxidation processes, Miner. Eng. 45 (2013) 88–93.

[7] A. Amrollahi, M. Massinaei, A. Zeraatkar Moghaddam, Removal of the residual xanthate from flotation plant tailings using bentonite modified by magnetic nanoparticles, Miner. Eng. 134 (2019) 142–155.

[8] S.H. Chen, W.Q. Gong, G.J. Mei, Q. Zhou, C.P. Bai, N. Xu, Primary biodegradation of sulfide mineral flotation collectors, Miner. Eng. 24 (8) (2011) 953–955.

[9] L. Li, M. He, Y.F. Feng, H.B. Wei, X.F. You, H. Yu, Q.B. Wang, J.X. Wang, Adsorption of xanthate from aqueous solution by multilayer graphene oxide: An experimental and molecular dynamics simulation study, Adv. Compos. Hybrid Mater. 4 (3) (2021) 725–732.

[10] C. Byrne, G. Subramanian, S.C. Pillai, Recent advances in photocatalysis for environmental applications, J. Environ. Chem. Eng. 6 (3) (2018) 3531–3555.

[11] X.G. Yang, D.W. Wang, Photocatalysis: From fundamental principles to materials and applications, ACS Appl. Energy Mater. 1 (12) (2018) 6657–6693.

[12] J. Schneider, M. Matsuoka, M. Takeuchi, J.L. Zhang, Y. Horiuchi, M. Anpo, D.W. Bahnemann, Understanding TiO_2 photocatalysis: Mechanisms and materials, Chem. Rev. 114 (19) (2014) 9919–9986.

[13] Q. Guo, C.Y. Zhou, Z.B. Ma, X.M. Yang, Fundamentals of TiO_2 photocatalysis: concepts, mechanisms, and challenges, Adv. Mater. 31 (50) (2019) 1901997.

[14] S. Peiris, H.B. de Silva, K.N. Ranasinghe, S.V. Bandara, I.R. Perera, Recent development and future prospects of TiO_2 photocatalysis, J. Chin. Chem. Soc. 68 (5) (2021) 738–769.

[15] C. Hu, J. Guo, J.H. Qu, X.X. Hu, Photocatalytic degradation of pathogenic bacteria with AgI/TiO_2 under visible light irradiation, Langmuir 23 (9) (2007) 4982–4987.

[16] J.H. Sun, L.P. Qiao, S.P. Sun, G.L. Wang, Photocatalytic degradation of Orange G on nitrogen-doped TiO_2 catalysts under visible light and sunlight irradiation, J. Hazard. Mater. 155 (1-2) (2008) 312–319.

[17] W.J. Lin, X.F. Xie, X. Wang, Y. Wang, D. Segets, J. Sun, Efficient adsorption and sustainable degradation of gaseous acetaldehyde and o-xylene using rGO-TiO_2 photocatalyst, Chem. Eng. J. 349 (2018) 708–718.

[18] V. Etacheri, C. Di Valentin, J. Schneider, D. Bahnemann, S.C. Pillai, Visible-light activation of TiO_2 photocatalysts: Advances in theory and experiments, J. Photochem. Photobiol. C Photochem. Rev. 25 (2015) 1–29.

[19] C.H. Nguyen, C.C. Fu, R.S. Juang, Degradation of methylene blue and methyl orange by palladium-doped TiO_2 photocatalysis for water reuse: Efficiency and degradation pathways, J. Clean. Prod. 202 (2018) 413–427.

[20] X.F. Qu, X.H. Zhao, M.H. Liu, Z.Q. Gao, D.L. Yang, L. Shi, Y.B. Tang, H.B. Song, BiOCl/TiO_2 composite photocatalysts synthesized by the sol–gel method for enhanced visible-light catalytic activity toward methyl orange, J. Mater. Res. 35 (22) (2020) 3067–3078.

[21] S. Liu, M. Lim, R. Amal, TiO_2-coated natural zeolite: Rapid humic acid adsorption and effective photocatalytic regeneration, Chem. Eng. Sci. 105 (2014) 46–52.

[22] H.L. Yang, Y. Wu, Z.W. Zhuang, Y. Li, C. Chen, Factors affecting the catalytic performance of nano-catalysts, Chin. J. Chem. 40 (4) (2022) 515–523.

[23] C.Q. Li, Z.M. Sun, A.K. Song, X.B. Dong, S.L. Zheng, D.D. Dionysiou, Flowing nitrogen atmosphere induced rich oxygen vacancies overspread the surface of TiO_2/kaolinite composite for enhanced photocatalytic activity within broad radiation spectrum, Appl. Catal. B Environ. 236 (2018) 76–87.

[24] K. Ullah, L. Zhu, Z.D. Meng, S. Ye, Q. Sun, W.C. Oh, A facile and fast synthesis of novel composite Pt–graphene/TiO_2 with enhanced photocatalytic activity under UV/Visible light, Chem. Eng. J. 231 (2013) 76–83.

[25] H. Dzinun, M.H.D. Othman, A.F. Ismail, Photocatalytic performance of TiO_2/Clinoptilolite: Comparison study in suspension and hybrid photocatalytic membrane reactor, Chemosphere 228 (2019) 241–248.

[26] C.C. Wang, Y. Zhan, Z.Y. Wang, TiO_2, MoS_2, and TiO_2/MoS_2 heterostructures for use in organic dyes degradation, ChemistrySelect 3 (6) (2018) 1713–1718.

[27] C.C. Wang, X. Wang, W. Liu, The synthesis strategies and photocatalytic performances of TiO_2/MOFs composites: A state-of-the-art review, Chem. Eng. J. 391 (2020) 123601.

[28] Y.F. Yang, L.D. Xu, H.F. Wang, W.J. Wang, L.X. Zhang, TiO_2/graphene porous composite and its photocatalytic degradation of methylene blue, Mater. Des. 108 (2016) 632–639.

[29] B. Szczepanik, Photocatalytic degradation of organic contaminants over clay-TiO_2 nanocomposites: a review, Appl. Clay Sci. 141 (2017) 227–239.

[30] P.F. Zhou, Y.B. Shen, S.K. Zhao, G.D. Li, B.Y. Cui, D.Z. Wei, Y.S. Shen, Synthesis of clinoptilolite-supported BiOCl/TiO_2 heterojunction nanocomposites with highly-enhanced photocatalytic activity for the complete degradation of xanthates under visible light, Chem. Eng. J. 407 (2021) 126697.

[31] H. Li, Y. Yao, X. Yang, X. Zhou, R. Lei, S. He, Degradation of phenol by photocatalysis using TiO_2/montmorillonite composites under UV light, Environ. Sci. Pollut. Res. Int 29 (45) (2022) 68293–68305.

[32] Y.H. Zhang, B.J. Miao, Q.L. Chen, Z.M. Bai, Y.G. Cao, B. Davaa, Synthesis, structure, and photocatalytic activity of TiO_2-montmorillonite composites, Catalysts 12 (5) (2022) 486.

[33] T.B.T. Dao, T.T.L. Ha, T. Do Nguyen, H.N. Le, C.N. Ha-Thuc, T.M.L. Nguyen, P. Perre, D.M. Nguyen, Effectiveness of photocatalysis of MMT-supported TiO_2 and TiO_2 nanotubes for rhodamine B degradation, Chemosphere 280 (2021) 130802.

[34] L.L. Yuan, D.D. Huang, W.N. Guo, Q.X. Yang, J. Yu, TiO_2/montmorillonite nanocomposite for removal of organic pollutant, Appl. Clay Sci. 53 (2) (2011) 272–278.

[35] K.E. Onwuka, K. Achilike, K.S. Eze, N.E. Enenwa, Montmorillonite clay enhanced TiO_2 nanoparticle for photocatalytic degradation of organic pollutants: Mini review, Int. J. Pharm. Sci. 1 (1) (2021) 33–38.

[36] K.K. Hu, L. E, D. Zhao, Y.J. Li, W. Zhao, H. Rong, Characteristics and performance of rutile/anatase/brookite TiO_2 and TiO_2–$Ti_2O_3(H_2O)_2(C_2O_4)\cdot H_2O$ multiphase mixed crystal for the catalytic degradation of emerging contaminants, CrystEngComm 22 (6) (2020) 1086–1095.

[37] H.F. Xu, G. Li, G. Zhu, K.R. Zhu, S.W. Jin, Enhanced photocatalytic degradation of rutile/anatase TiO_2 heterojunction nanoflowers, Catal. Commun. 62 (2015) 52–56.

[38] S. Bagheri, N.M. Julkapli, Mixed-phase TiO_2 photocatalysis: correlation between phase composition and photodecomposition of water pollutants, Rev. Inorg. Chem. 37 (1) (2017) 11–28.

[39] V. Likodimos, A. Chrysi, M. Calamiotou, C. Fernández-Rodríguez, J.M. Doña-Rodríguez, D.D. Dionysiou, P. Falaras, Microstructure and charge trapping assessment in highly reactive mixed phase TiO_2 photocatalysts, Appl. Catal. B Environ. 192 (2016) 242–252.

[40] M.E. Bustos, F. Hevia, S. Fuentes, A.I. Martínez, R.A. Zárate, A novel route for the preparation of self-assembled CuO hierarchical nanostructures by hydrothermal processing at high pressure, Mater. Lett. 297 (2021) 129936.

[41] W.B. Liu, X.Y. Peng, W.G. Liu, K.L. Tong, Y.B. Shen, Q. Zhao, S.K. Zhao, W.H. Sun, Novel polyhydroxy cationic collector N-(2,3-propanediol)-N-dodecylamine: Synthesis and flotation performance to hematite and quartz, Int. J. Min. Sci. Technol. 33 (1) (2023) 115–122.

[42] P.F. Zhou, Y.B. Shen, S.K. Zhao, J.Z. Bai, C. Han, W.G. Liu, D.Z. Wei, Facile synthesis of clinoptilolite-supported Ag/TiO_2 nanocomposites for visible-light degradation of xanthates, J. Taiwan Inst. Chem. Eng. 122 (2021) 231–240.

[43] J. Liu, J. Jin, Z. Deng, S.Z. Huang, Z.Y. Hu, L. Wang, C. Wang, L.H. Chen, Y. Li, G. Van Tendeloo, B.L. Su, Tailoring CuO nanostructures for enhanced photocatalytic property, J. Colloid Interface Sci. 384 (1) (2012) 1–9.

[44] S. Harish, J. Archana, M. Sabarinathan, M. Navaneethan, K.D. Nisha, S. Ponnusamy, C. Muthamizhchelvan, H. Ikeda, D.K. Aswal, Y. Hayakawa, Controlled structural and compositional characteristic of visible light active ZnO/CuO photocatalyst for the degradation of organic pollutant, Appl. Surf. Sci. 418 (2017) 103–112.

[45] P. Apopei, C. Catrinescu, C. Teodosiu, S. Royer, Mixed-phase TiO_2 photocatalysts: crystalline phase isolation and reconstruction, characterization and photocatalytic activity in the oxidation of 4-chlorophenol from aqueous effluents, Appl. Catal. B Environ. 160-161 (2014) 374–382.

[46] S.K. Zhao, Y.B. Shen, P.F. Zhou, J. Zhang, W. Zhang, X.X. Chen, D.Z. Wei, P. Fang, Y.S. Shen, Highly selective NO_2 sensor based on p-type nanocrystalline NiO thin films prepared by sol–gel dip coating, Ceram. Int. 44 (1) (2018) 753–759.

[47] J.H. Lee, J.H. Kim, S.S. Kim, CuO–TiO_2 p–n core–shell nanowires: sensing mechanism and p/n sensing-type transition, Appl. Surf. Sci. 448 (2018) 489–497.

[48] Y.J. Wang, Q.S. Wang, X.Y. Zhan, F.M. Wang, M. Safdar, J. He, Visible light driven type II heterostructures and their enhanced photocatalysis properties: a review, Nanoscale 5 (18) (2013) 8326–8339.